A Hybrid Model Framework for the Optimization of Preparative Chromatographic Processes

Deepak Nagrath, Achille Messac,† B. Wayne Bequette, and S. M. Cramer*

Howard P. Isermann Department of Chemical Engineering, Rensselaer Polytechnic Institute, Troy, New York 12180-3590

An optimization framework based on the use of hybrid models is presented for preparative chromatographic processes. The first step in the hybrid model strategy involves the experimental determination of the parameters of the physical model, which consists of the full general rate model coupled with the kinetic form of the steric mass action isotherm. These parameters are then used to carry out a set of simulations with the physical model to obtain data on the functional relationship between various objective functions and decision variables. The resulting data is then used to estimate the parameters for neural-network-based empirical models. These empirical models are developed in order to enable the exploration of a wide variety of different design scenarios without any additional computational requirements. The resulting empirical models are then used with a sequential quadratic programming optimization algorithm to maximize the objective function, production rate times yield (in the presence of solubility and purity constraints), for binary and tertiary model protein systems. The use of hybrid empirical models to represent complex preparative chromatographic systems significantly reduces the computational time required for simulation and optimization. In addition, it allows both multivariable optimization and rapid exploration of different scenarios for optimal design.

1. Introduction

Currently, several well-developed mathematical approaches exist for the optimization of chromatographic processes. Most of these approaches have been restricted to the use of physical models that are based on the standard transport and thermodynamic descriptions of these systems (Gallant et al., 1996; Natarajan et al., 2000b; Guiochon et al., 1994). Felinger and Guiochon (1993 and 1996) used a simplex-based technique to maximize production rates in overloaded elution and displacement chromatography for a Langmuirian isotherm. Suwondo et al. (1993) employed a generalized reduced gradient method to maximize throughput in ideal linear chromatography. Felinger and Guiochon (1996) suggested the use of the product of production rate and yield as an alternative objective function. Luo and Hsu (1997) used an iterative scheme to optimize the gradient slope in nonideal, linear ion exchange protein chromatography. In addition, we have developed iterative optimization schemes for step (Gallant et al., 1995), linear gradient (Gallant et al., 1996), and displacement systems (Natarajan et al., 2000). All of the current optimization approaches (Gallant et al., 1995a; Gallant et al., 1996; Natarajan et al., 2000; Felinger and Guiochon, 1996; Suwondo et al., 1993) either use a single variable optimization and/or are unfavorable for exploration of different design scenarios. Moreover, these approaches employ physical models that are typically represented by coupled partial differential equations, making nonlinear multivariable optimization computationally expensive. Clearly, there is a need to develop more efficient strategies for chromatographic optimization.

Even though a sustained effort has been made toward development of comprehensive first principles models that can describe mass transfer and kinetics of biomolecules in chromatographic processes, the application of these models in multivariable optimization is hampered by a lack of a computationally economical framework.

Major advances in the area of high-speed parallel computing and development of faster computers in recent years has produced significant increases in the usage of *in silico* predictions and large-scale optimization for various applications. In the current work, we employ high-speed computing to carry out a large number of simulations with the physical model (described below) to obtain the data required to generate neural-network-based empirical models. The motivation for the use of both physical and empirical models is to complement the knowledge of the physics from the physical model with the simplicity and low computational cost of the empirical model. Hence, the hybrid model formulation has the advantages of both physical and empirical modeling approaches. Although empirical models can be generated for various experimental systems, they typically require a significant number of experiments in order to build a reliable multivariable model. On the other hand, physical models have the advantage of requiring relatively few experiments for parameter estimation but are computationally expensive. The strategy presented in this paper permits the development of a functional relationship between decision variables (e.g., gradient slope, flow rate, feed load for gradient separations) and the objective functions (e.g., production rate, yield, maximum solute concentration), resulting in the development of a lower-level algebraic model that can be rapidly optimized.

* To whom correspondence should be addressed. Ph: (518) 276-6198. Fax: (518) 276-4030. Email: crames@rpi.edu.

† Department of Mechanical, Aeronautical and Nuclear Engineering, Rensselaer Polytechnic Institute.

10.1021/bp034026g CCC: $27.50
Published on Web 11/14/2003

Table 1. Issue-Based Comparison of Physical-Model-Based Optimization with Hybrid-Model-Based Optimization

issues	physical model	hybrid model
number of design parameters	critical issue	nonissue
operating conditions identification	critical issue (order $\sim n$ to n^2)	nonissue
exploration of different scenarios	highly impractical for realistic n	nearly trivial
function evaluations	minutes-hours	seconds
use of complex models	practically prohibitive	permissible due to parallelization

Table 1 summarizes the advantages of the hybrid model for optimization by comparing it with the traditional physical-model-based optimization approach. For example, dealing with a large number of decision variables is a critical issue for physical-model-based optimization, whereas it is not an issue for hybrid-model-based optimization. This is because the total number of Jacobian evaluations is proportional to the number of design parameters. Although the identification of optimal operating conditions for a large number of objective functions and constraints is a critical issue for physical-model-based optimization, it is a nonissue for hybrid-model-based optimization (Nagrath et al., 2002) due to the optimization of relatively simple algebraic relationships. One of the most important advantages of hybrid-model-based optimization is the ability to explore different design scenarios (Nagrath et al., 2002) without any additional computational requirements. This is impractical for physical-model-based optimization strategies because each exploration requires re-optimization. In addition, a hybrid model framework permits the straightforward coupling of optimal column design with optimal operating conditions, under different parametric specifications. Finally, the computational time for each function evaluation is in minutes-hours for physical-model-based optimization, whereas it is seconds for the hybrid model strategy.

In the current work, hybrid models are developed for binary (α chymotrypsinogen A and ribonuclease A) and tertiary (α chymotrypsinogen A, ribonuclease A, and an artificial component) model systems. The parameters of the physical model (the general rate model coupled with the kinetic form of the steric mass action isotherm) are experimentally determined and then used to carry out a set of simulations with the physical model to obtain data on the functional relationship between various objective functions and decision variables. The resulting data is then used to estimate the parameters for neural-network-based empirical models. The resulting empirical models are then used with a sequential quadratic programming optimization algorithm to maximize the objective function, production rate times yield (in the presence of solubility and purity constraints), for binary and tertiary model protein systems. Finally, we employ this hybrid modeling approach for simultaneous optimal column design and identification of optimal operating conditions at various purity levels.

2. Theory

A. Physical Model. The physical model used in this work is the general rate model, which includes parallel diffusive (solid and pore diffusion) transport. The parallel diffusive model has been earlier applied for small molecules to predict column breakthrough profiles (Ma et al., 1997) and uptake adsorption analysis (Saunders et al., 1989). Yoshida et al. (1994) utilized a parallel diffusive model for uptake analysis of BSA using the Langmuir isotherm. Ernest et al. (1998) coupled the general rate model with the stoichiometric displacement isotherm for small molecules in an ion-exchange setting. In the current article, the general rate model is coupled with the kinetic form of steric mass action (SMA) isotherm. The presented SMA model accounts for *both* the effect of salt on the adsorption of biomolecules *and* the effect of the steric shielding, which occurs during the binding of large molecules to ion-exchange surfaces.

In the general rate model, the transport processes occurring in the bulk phase (eqs 1−3) are convection along the column axial direction, axial dispersion, and transport of solute by film transfer from the bulk phase to the intraparticle surface.

$$\frac{\partial c_i}{\partial t} = D_{ai}\frac{\partial^2 c_i}{\partial x^2} - u_o\frac{\partial c_i}{\partial x} - \frac{(1-\epsilon_i)}{\epsilon_i}\frac{3k_{fi}}{R}[c_i - c_{pi}(r=R)] \quad (1)$$

Initial and boundary conditions:

$$c_i = c_i(0, x)\ i = 1, 2, ..., N \quad (2)$$

$$Da_i\frac{\partial c_i}{\partial x} = \begin{cases} \begin{bmatrix} 0 & x = L \\ u_o[c_i - c_{fi}(t)] & x = 0 \end{bmatrix}; i = 1, 2, ..., N \end{cases} \quad (3)$$

The mass balance in the pore phase (eqs 4 and 5) can be represented by the Fickian diffusion and the slow adsorption−desorption (nonequilibrium kinetics) at the adsorption sites:

$$\frac{\partial c_{pi}}{\partial t} = D_{pi}\frac{1}{r^2}\frac{\partial\left[r^2\frac{\partial c_{pi}}{\partial r}\right]}{\partial r} - \frac{1-\epsilon_p}{\epsilon_p}y_{li}$$

$$i = 1...N \quad (4)$$

Initial and boundary conditions:

$$c_{pi} = c_{pi}(0, r) \quad (5)$$

$$\epsilon_p D_{pi}\frac{\partial c_{pi}}{\partial r} + (1-\epsilon_p)D_{si}\frac{\partial q_i}{\partial r} = k_{fi}(c_i - c_{pi});\ r = R \quad (6)$$

$$\frac{\partial c_{pi}}{\partial r} = 0;\ r = 0 \quad (7)$$

The mass balance in the solid phase (eqs 8 and 9) is due to adsorption−desorption and surface diffusion (hopping of molecules on adsorption sites) in the solid phase.

$$\frac{\partial q_i}{\partial t} = D_{si}\frac{1}{r^2}\frac{\partial\left[r^2\frac{\partial q_i}{\partial r}\right]}{\partial r} + y_{li};\ i = 2...N \quad (8)$$

$$q_i = q_i(0,r) \quad (9)$$

$$\frac{\partial q_i}{\partial t} = 2D_{si}\frac{\partial q_i}{\partial r} + y_{li};\ r = R \quad (10)$$

$$\frac{\partial q_i}{\partial r} = 0;\ r = 0 \quad (11)$$

where y_{li} is the net rate of adsorption−desorption.

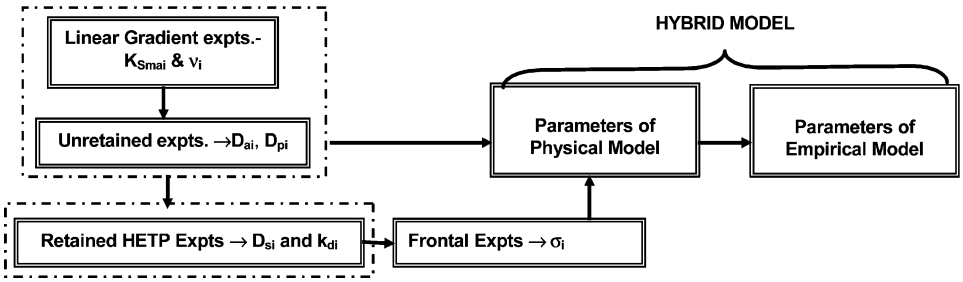

Figure 1. Generation of hybrid model.

Steric Mass Action Based Kinetic Model. The steric mass action (SMA) formalism accounts for *both* the effect of salt on the adsorption of biomolecules *and* the effect of the steric shielding, which occurs during the binding of large molecules to ion-exchange surfaces. A detailed account of the SMA isotherm is presented elsewhere (Brooks and Cramer, 1992). Briefly, in the formulation presented here, we take into account the nonlinear, nonequilibrium kinetics.

$$c_{pi} + \nu_i \bar{q}_1 \Leftrightarrow q_{pi} + \nu_i c_{p1};\ i = 2...N \tag{12}$$

The adsorption−desorption process for proteins can be represented as shown in eq 12. The net rate of adsorption−desorption is

$$y_{li} = k_{ai} c_{pi} \bar{q}_1^{\nu_i} - k_{di} q_{pi} c_1^{\nu_i} \tag{13}$$

At any time, electroneutrality must be satisfied on the stationary phase in the following manner:

$$\bar{q}_1 = \Lambda - \sum_{i=2}^{N} (\upsilon_i + \sigma_i) q_i \tag{14}$$

To model the mass transport of salt in the axial direction and pore phase, eqs 1−7 are used; however, for the mass balance of salt in the solid phase, the electroneutrality condition is used to estimate q_1 as follows:

$$q_1 = \Lambda - \sum_{i=2}^{N} (\upsilon_i) q_i \tag{15}$$

where $q_1 = \bar{q}_1 + \sum_{i=2}^{N} (\sigma_i) q_i$ is the total bound concentration of salt on the stationary phase. The boundary condition for salt in the solid phase (at the particle surface) is estimated implicitly by calculating the net rate of accumulation of proteins in the stationary phase at the particle surface and can be represented as

$$\sum_{i=2}^{N} \nu_i \frac{\partial q_i}{\partial t} = 2 D_{s1} \frac{\partial q_1}{\partial r} \tag{16}$$

It was observed that the electroneutrality is strictly conserved with this approximation.

B. Generation of Hybrid Model. The schematic for generating the hybrid model is shown in Figure 1. In the hybrid model, the physical model is used for the parametric simulations to generate *n*-dimensional response surfaces, which relate the production rate, yield, and purity to the other parameters of the system (e.g., feed load, flow rate, salt gradient). The *first step* in the generation of the hybrid model, as shown in Figure 1, is to determine adsorption isotherm and transport parameters using analytical chromatographic experiments. The adsorption isotherm that is employed for this work is the steric mass action (SMA) isotherm described in the previous section. Linear isotherm parameters (K_{smai}, ν_i) are first obtained by linear gradient experiments (Gallant et al., 1995). The axial dispersion coefficient (D_{ai}) and pore diffusion coefficient (D_{pi}) are then obtained by unretained height equivalent theoretical plate (HETP) chromatographic experiments (Natarajan and Cramer, 2000a). The surface diffusion coefficient (D_{si}) and desorption rate constant k_{di} are then determined from retained HETP experiments. Finally, the steric factor is obtained from frontal experiments for the model feed mixtures.

These experiments provide us with an initial set of parameters for the physical model that is then used for the generation of the empirical model. The combined strategy is defined as a hybrid model to differentiate this approach from empirical models derived solely from experimental data. Thus, the empirical model will essentially be a mathematical representation of the response surfaces. This approach eliminates the need for a large number of preparative chromatographic experiments to train the model and offers an opportunity to update the empirical model with real experimental data (Nagrath et al., 2003). Because the data is generated over a wide range of input-output space, the hybrid model will be applicable for the whole design space from which optimal design parameters are selected. The multi-input (e.g., feed load, flow rate, salt gradient, length), multi-output (production rate, yield, maximum solute concentration) empirical model for ion exchange processes is generated from large sets of data obtained from simulations using the physical model.

C. Data Generation. As indicated above, the physical model is used for parametric simulations to generate *n*-dimensional response surfaces, which relate the production rate, yield, and maximum solute concentration to the decision variables of feed load, flow rate, initial salt concentration, and gradient slope (for gradient chromatography), subject to purity as a constraint. The decision variables are simultaneously varied using random Gaussian signals (zero mean, finite variance perturbations), and the corresponding outputs are determined from the simulations obtained with the physical model. The simulations employ parallel computing to enable a large number of simulations to be carried out in a reasonable time. The extensive data generation for the empirical optimization model is done efficiently by coupling message passing interface (MPI) subroutines in the general rate model serial code (written in Fortran 90 to enable parallel computing and to reduce memory allocation). MPI is a published standard that defines the calling sequences and behavior of the routines in the message-passing library. The parallel version of the code then runs under the control of a parallel run-time system that allocates processors to the task. The parameter and operating spaces are judiciously divided between different processors. Each processor then runs the same code with a different parameter space and operating conditions and

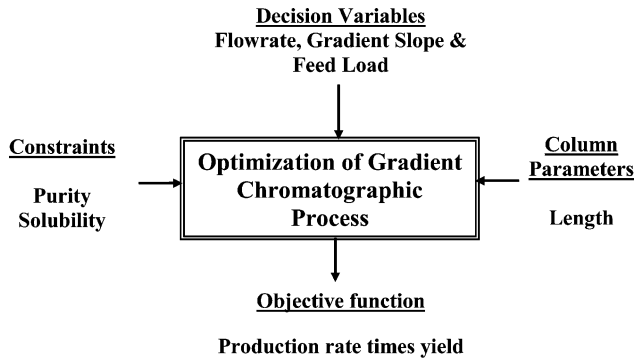

Figure 2. Schematic showing variables involved in optimization of linear gradient chromatographic processes.

communicates with each other at the end of the runs to combine the data generated using individual processors. The simulations are performed on 48 Netra X1 node Sun Beowulf Cluster at Scientific Centre for Research & Computing (SCOREC), RPI.

The outputs that are obtained from the simulations are the maximum concentration of a solute, production rate, and yield at various levels of purity.

D. ANN Empirical Model. The data are then used to develop the multi-input, multi-output empirical model using multilayer artificial neural networks (ANN). The main advantage of ANN-based models is the extreme flexibility and capacity to adequately represent nonlinear systems of high complexity. The generated empirical models are validated using a representative data set. The hybrid empirical models are then used in nonlinear optimization to obtain the optimum operating conditions for the process. The computational cost is significantly less for the optimization of processes modeled by the ANN-based models as compared with using the fundamental physical models.

3. Numerical Method

A. Physical Model. The spatial discretization of the bulk phase was done using the Galerkin finite element formulation (Gu et al., 1990). The approach of the Galerkin finite element method is to solve the system of equations in residual form until the residuals are zero. The differential form of the bulk phase eq 4 given above assumes that the solutions variables can be expanded in Taylor's series and therefore are smooth functions with respect to space and time. However, in the presence of sharp discontinuities, the solution lacks the sufficient smoothness requirements and the differential form cannot be applied. Hence, a more basic form of the equation, the weak form, which decreases the continuity requirements of the solution, was utilized. The dimensionless form of the transport equations and their discretized form are presented in the Appendix. The axial dimensionless length is divided into 110 finite elements, and piece-wise quadratic shape functions were used to interpolate the solution over each element domain.

For the particle phase transport, the equations were discretized using the orthogonal collocation on finite elements. Lagrange polynomials were used as the trial functions. Orthogonal collocation was applied over each element (maximum number of elements was 3), and the continuity requirement was applied over each intersecting boundary of an element. At the particle boundary (at the center and the surface of a spherical particle), boundary conditions (6−7 and 10−11) were employed. Collocation points used in this work are the roots of the orthogonal Legendre polynomial. The collocation matrices (*A* and *B*, eqs 26 and 27, respectively) were calculated using the quadrature rule employing a Lagrange polynomial as the trial functions. The formulation chosen for calculation of these matrices preserves the orthogonality of each trial function.

The above discretized particle phase equations were then coupled with the discretized bulk phase equations. The concentration variables were assembled element by element and solved simultaneously using a differential algebraic solver. The element assembly procedure remains the same irrespective of the discretization procedure being used in the axial domain.

The above discretized bulk phase ordinary differential equations were solved simultaneously with the particle phase equations (which are discretized using the orthogonal collocation on finite elements) using the differential algebraic solver DDASPK (Petzold, 1982).

B. Empirical Model. In ANN topology, each element of input vectors are connected to each neuron in the input

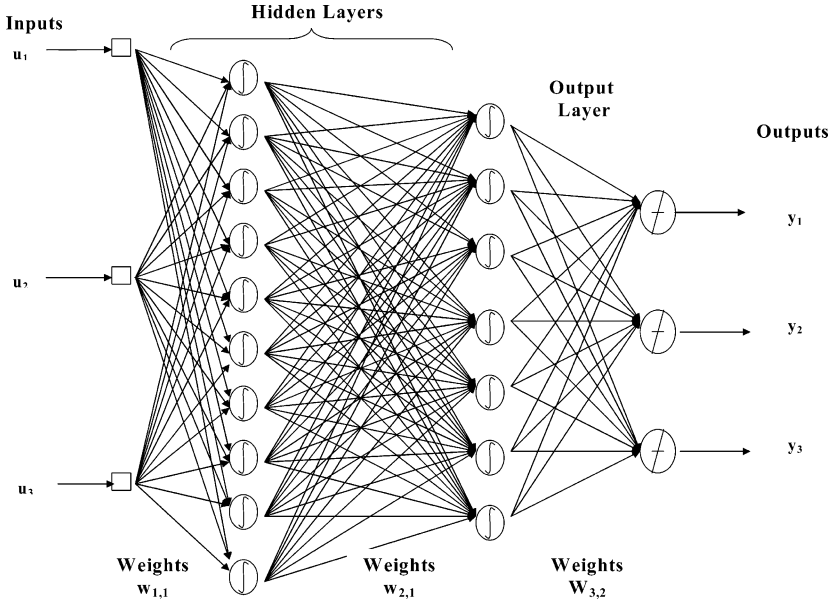

Figure 3. Typical neural network architecture connecting variables of a particular component in the current work for a 3 input-3 output system.

Table 2. Mass Transfer, Isotherm, and Column and Resin Parameters on FF Sepharose (90 μm)

Mass Transfer Parameters

proteins	D_P (cm^2/s)	D_s (cm^2/s)	$3k_f$ L/R (s^{-1})	ζ (cm)
α chymotrypsinogen	2.9×10^{-7}	1.45×10^{-8}	5	1.5×10^{-2}
ribonuclease	3.2×10^{-7}	4.8×10^{-8}	5	3.3×10^{-2}
artificial component	2.5×10^{-7}	1.45×10^{-8}	5	1.4×10^{-2}

Isotherm Parameters

proteins	k_d (mM$^{-\nu}$/s)	K_{SMA}	σ	ν
α chymotrypsinogen	1.5×10^{-7}	0.0039	10	4.4
ribonuclease	5.4×10^{-6}	0.0077	10	3.7
artificial component	2.0×10^{-7}	0.0039	10	4.7

Column and Resin Parameters

proteins	ϵ_i	ϵ_p	ϵ_t	D (cm)	L (cm)	Λ
α chymotrypsinogen	0.31	0.68	0.7792			
ribonuclease	0.31	0.68	0.7792	1.6	10.5	1200
artificial component	0.31	0.68	0.7792			

layer through the modifiable weights in the weight matrix $w_{i,j}$. The inputs to each neuron are summed through a summing junction, and the output of each neuron is obtained by using a *sigmoidal* transfer function (other transfer functions such as *linear*, *tanh* could also be used) over the weighted summed input. Finally, the neuron layer outputs are either connected to output neurons (for a single layer network) or to another layer of neurons in a hidden layer (for multilayer networks). Figure 3 shows the schematic for a two-hidden-layer multilayer perceptron. The case shown is a representative one, having three input and three output vectors. In the output layer, hidden neurons are connected to the output vectors. In addition, there is a bias node in each hidden layer, which is connected to the next layer neurons. Hence, for the particular case shown in Figure 3, there are two hidden layers and an output layer. The first and second hidden layers have 10 and 7 neurons, respectively. The transfer function employed for hidden layers in the current work is the sigmoidal function, and for the output layer linear transfer function is utilized. Using linear transfer function in the output layer helps in estimating the data beyond the range. For clarity, in the figure bias nodes are not shown. The weight matrices are denoted by $w_{i,j}$. Here index i and j denote the destination and source layer, respectively.

The innate problem in neural network is the generalization to unseen data. The generalization is essential because generally a training error can be decreased to a small value; however, for a new data that were not used to train the network, the error can still be large. The simplest way to avoid this overfitting is by increasing the size of the training set. For many applications, there are limitations to increasing the data because of economics and time. Fortunately, this is not an issue in the current work since a parallel computing environment is used for the simulations, and the supply of data is limited only to the number of available nodes in the parallel cluster.

To achieve a good generalization, in the current work, increasing the amount of data was not the only mechanism adopted. We can find in the literature several approaches (e.g., early stopping, regularization, jittering, etc.) to avoid overfitting, each having their own merits. We first explored all the three mentioned approaches; however, after extensive study we found that Bayesian regularization gives better generalization performance than the early stopping for our system. Hence, in the current work, we have implemented Bayesian regularization and jittering to improve generalization. In Bayesian regularization, both the mean of sum of squares of network weights and network errors are minimized as shown in eq 17, and the weights and regularization parameter (γ) are estimated in an automated fashion using statistical techniques. The detailed procedure is given in MacKay (1992).

$$MSEREG = \gamma\frac{1}{N}\sum_{i=1}^{N}(e_i)^2 + (1-\gamma)\frac{1}{n}\sum_{j=1}^{n}(w_j)^2 \quad (17)$$

In the current work, the data obtained from the physical model is first preprocessed so that it falls within a [−1, 1] range. The preprocessed data is then divided into two data sets, training and test set. The training data set is used to train the network, and the test data set is used to estimate the generalization error of the network. The high-performance fast training procedure, Levenberg−Marquardt backpropogation, which is based on nonlinear optimization, is used for training the network. Since it is important for Bayesian regularization that the network be trained until sum squared error, sum squared weights, and the effective number of parameters attain constant values (which essentially indicates that the network has attained convergence), the network was trained until the convergence was achieved. Since the outputs of the generated networks fall in the [−1, 1] range, the network outputs are postprocessed to convert the data back into the physical units. All the future inputs are first preprocessed with the same parameters, which were used to generate the network, and then are sent as input to the network.

The middle eluting component (for the tertiary system studied in this paper) generally experiences overlap from both the early and later eluting components at higher feed load conditions. Since the estimated yield and production rate may essentially be zero (if purity constraints are not satisfied), a separate set of simulations were performed under milder conditions to generate effective data for modeling the middle eluting component.

4. Results and Discussion

Figure 2 presents the variables involved in a typical optimization of linear gradient chromatography. The decision variables are the parameters over which the designer has direct control. For gradient separation systems these variables are typically flow rate, gradient slope, and feed load. While a wide variety of objective functions have been employed in preparative chromatographic separations, the most common objective function to date has been the production rate, which is defined as the amount of product produced at a given level of purity per unit time, per unit volume of stationary phase

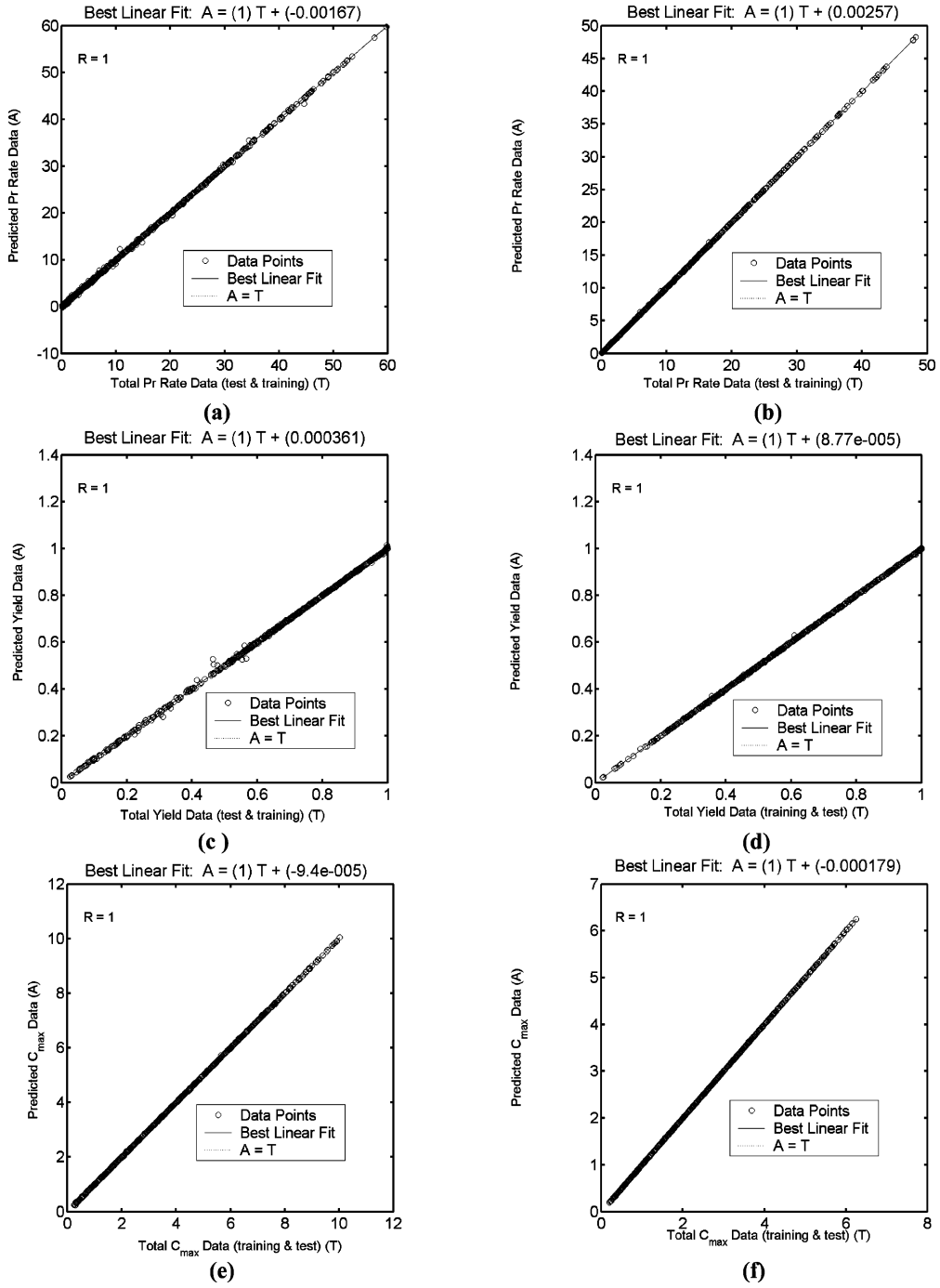

Figure 4. Prediction capability of the generated hybrid empirical models for early and later eluting component is shown for total data (training and test). Prediction for production rates of early and later eluting components are shown in (a) and (b), respectively. Yield predictions for early and later eluting components are shown in (c) and (d), respectively. Maximum solute concentration predictions for early and later eluting components are shown in (e) and (f), respectively.

material. Natarajan et al. (2000) have optimized the production rate using yield as a constraint. Although this method improves the production rate and satisfies the yield as a hard constraint, it leads to an inflexible setting. In other words, this approach provides minimal flexibility to the chromatographic engineer who may desire to use yield as a soft constraint. Felinger and Guiochon (1996) suggested using the product of production rate and yield as an alternative objective function. In this work, we have employed the product of production rate and yield as the objective function. In preparative systems, there are hard constraints that have to be met to provide a realistic estimate of the achievable production rate of a separation. In the current work, solubility and purity are used as hard constraints and column length is used as the column design parameter. Note: For the simulations in the current work, an initial salt concentration of 50 mM was employed. Further, the separation time was determined by the time required to completely elute the most retained component.

The transport and kinetic parameters for the proteins α chymotrypsinogen A and ribonuclease A were obtained as described previously (Natarajan et al., 2002) and are shown in Figure 2. In that paper, it was demonstrated that the predictions obtained from the physical model corresponded well with the experiments. In the current article, we first investigate the linear gradient separation of a binary model protein mixture (α chymotrypsinogen

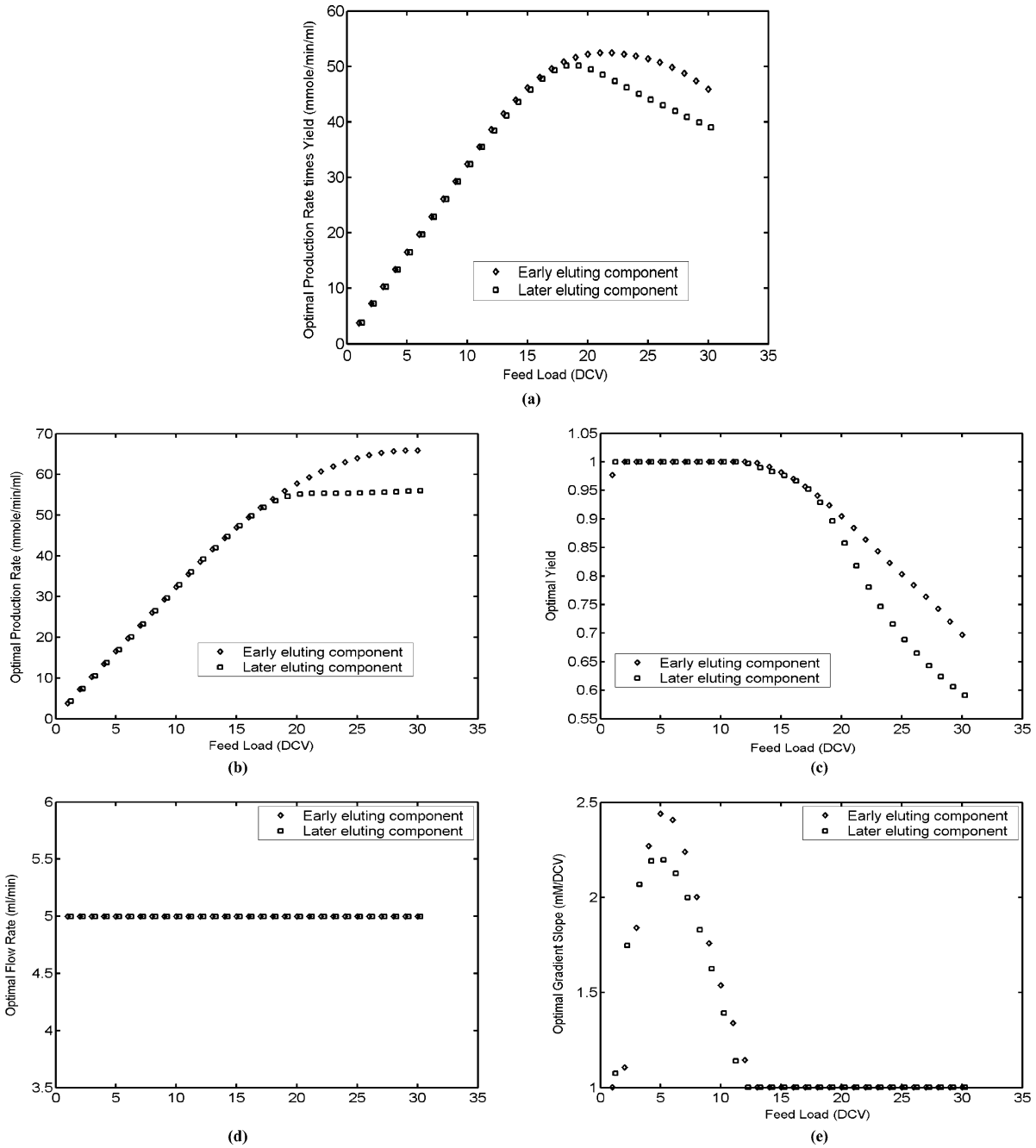

Figure 5. Optimization results for two model proteins, α chymotrypsinogen A and ribonuclease A on 90 μm FF Sepharose stationary phase. Column conditions: diameter 1.6 cm; length 10.5 cm. Feed conditions: ribonuclease A and α chymotrypsinogen A at 0.7 mM each. (◊) Results for early eluting components. (□) Results for later eluting components. All optimal results are presented as a function of column loadings (DCV). (a) Optimal production rate times yield (mmol/min/mL). (b) Optimal production rate (mmol/min/mL). (c) Optimal yield. (d) Optimal flow rate (mL/min). (e) Optimal gradient slope (mM/DCV). Here DCV, denotes the dimensionless column volume.

A and ribonuclease A). To examine a more complex separation, a ternary mixture consisting of α chymotrypsinogen A, ribonuclease A, and a later eluting artificial component is then investigated at constant (95%) and varying (91%, 95% and 99%) levels of purity. The isotherm and transport parameters of the artificial component is chosen in such a manner that a relatively low separation factor (1.33) is maintained between the middle eluting α chymotrypsinogen A and the later eluting artificial component (note: the average separation factor between α chymotrypsinogen A and ribonuclease A is 1.54). The resulting mass transfer, isotherm, and column parameters for all three components are presented in Table 2.

Finally, we employ the hybrid modeling approach for simultaneous optimal column design and identification of optimal operating conditions at various purity levels. In all of the cases examined in this article, the solubility constraint is satisfied using a hard constraint on the maximum solute concentration of 5 mM.

A. Binary Systems. This section presents the optimization results for the linear gradient separation of a binary protein mixture (α chymotrypsinogen A and ribonuclease A). We first develop the ANN-based hybrid models for both components as described in the theory section and then use them in SQP-based optimization. Figure 4 shows that the generated hybrid models have excellent predictive ability for outputs (production rate,

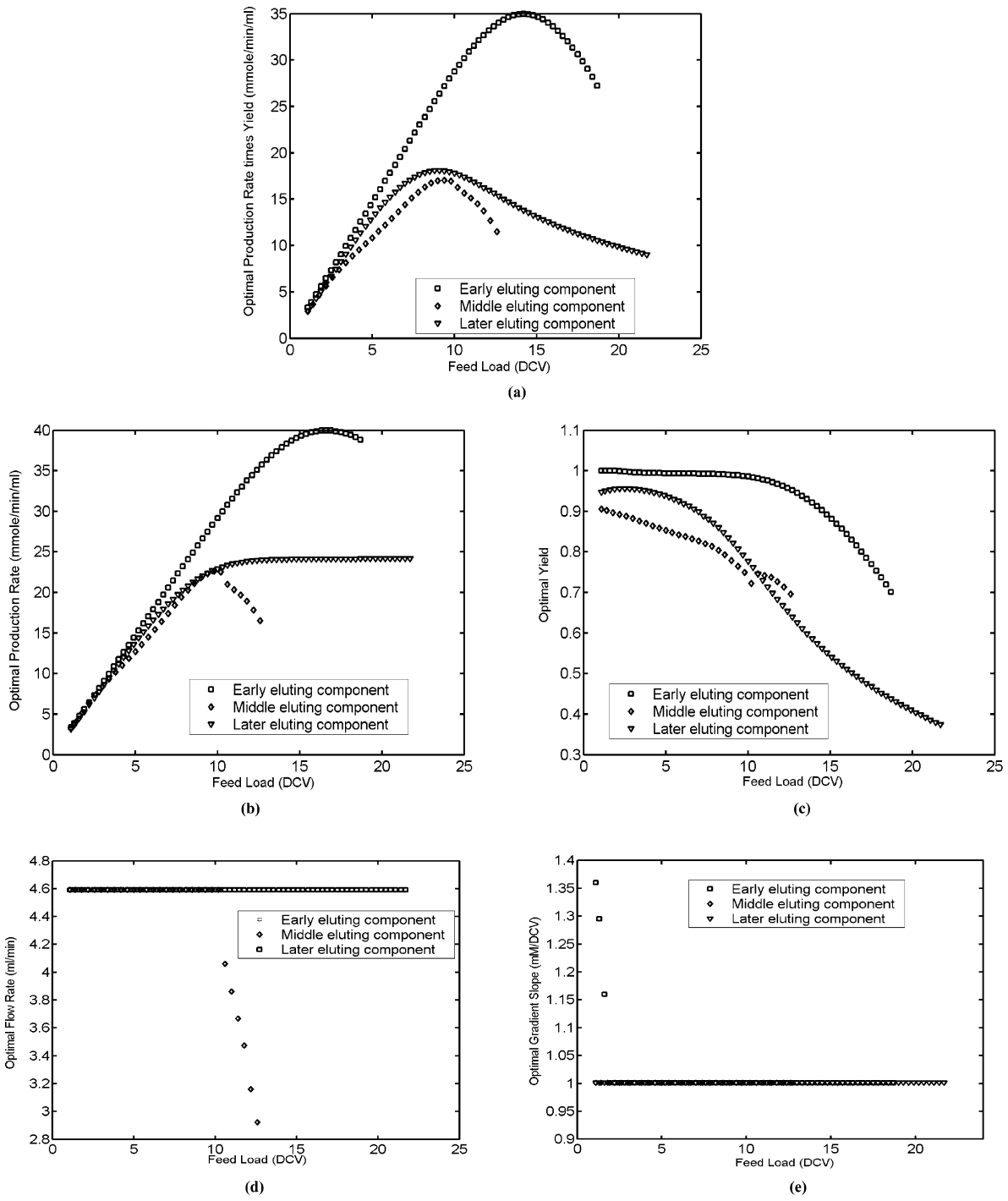

Figure 6. Optimization results for a tertiary mixture (α chymotrypsinogen A, ribonuclease A, and artificial component) on a 90 μm FF Sepharose stationary phase. (□) Results for early eluting component (ribonuclease A). (◊) Results for middle eluting component (α chymotrypsinogen A). (▽) Results for later eluting component (artificial). Column conditions: diameter 1.6 cm; length 10.5 cm. Feed conditions: ribonuclease A, α chymotrypsinogen A, and the artificial component at 0.5 mM each. The average separation factor is 1.55 between ribonuclease A and α chymotrypsinogen A and 1.35 between α chymotrypsinogen A and the artificial eluting component. All optimal results are presented as a function of column loadings (DCV). (a) Optimal production rate times yield (mmol/min/mL). (b) Optimal production rate (mmol/min/mL). (c) Optimal yield. (d) Optimal flow rate (mL/min). (e) Optimal gradient slope (mM/DCV).

yield, and maximum solute concentration) of both components. As seen in the figure, yield data (and correspondingly the production rate) was obtained over a very wide range (from 10% to 100%). This ensures the accurate mapping of the whole design space of interest for optimization.

Figure 5a illustrates the variation of the optimum production rate times yield as a function of feed load for the early and later eluting components. The corresponding optimum values of production rate, yield, gradient slope and flow rate are shown in Figure 5b−e, respectively. Several observations can be made from the figures. The maximum of the production rate times yield for the later eluting component occurs at a lower column loading than that for the early eluting component. In addition, the optimum value of production rate times yield is higher for the early eluting component than the later eluting component. The corresponding optimal values of the production rates are higher for the early eluting component. It can be seen that at higher loadings there

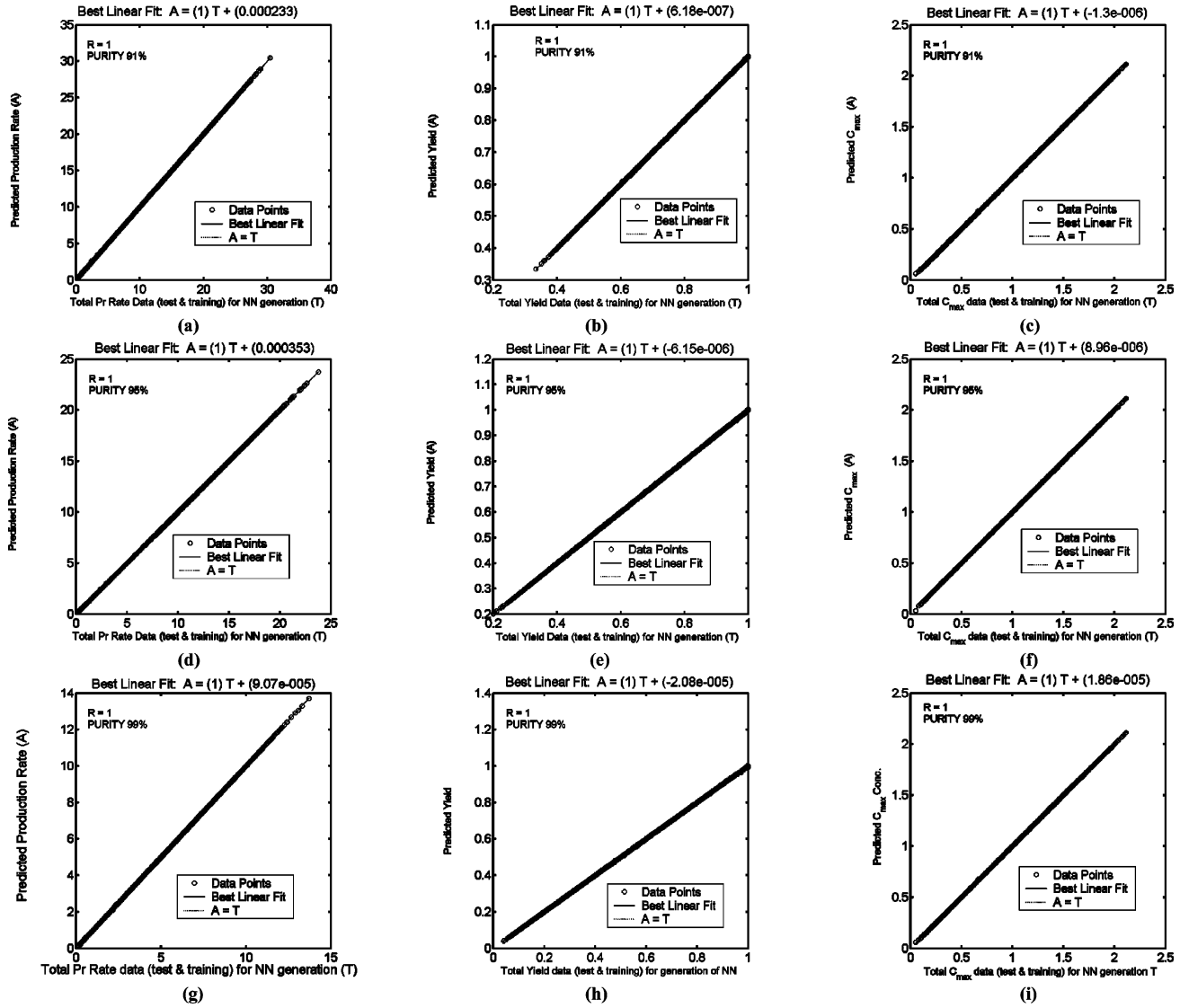

Figure 7. Prediction capability of the generated hybrid empirical models for total data (training and test) at three different purity levels (91%, 95%, and 99%) for the later eluting component. Prediction for production rates, at 91%, 95%, and 99% purity levels for later eluting component are shown in (a), (d), and (g), respectively. Yield predictions at 91%, 95%, and 99% purity levels for later eluting components are shown in (b), (e), and (h), respectively. Maximum solute concentration predictions at 91%, 95% and 99% purity levels for later eluting components are shown in (c), (f), and (i), respectively.

is a relatively sharp decrease in the yield of the later eluting component. In addition, the optimum flow rate is relatively independent of the loading for both early and later eluting components. The optimal gradient slope first increases, then decreases with increased loading, and finally remains at a constant lower value for higher loadings.

At any feed load, as the gradient slope becomes higher, there is an increased mixed zone between closely retained components that decreases both the yield and purity of the desired component. Under low to moderate feed load conditions, production rate increases when loading is increased. At high loading conditions, sample displacement effects can become pronounced, resulting in significant narrowing of the bands. For relatively low separation factor systems, any increase in the gradient slope can result in losses of material because the narrowing of the bands results in losses due to shock layer effects in these induced sample displacement systems (Nagrath et al., 2002). Hence, increase in the loading necessitates lowering of the gradient slope. The optimal flow rate is the highest for all of the loadings because the higher production rate attained at higher flow rates overshadowed any adverse transport effects for this particular separation.

B. Tertiary Systems. ***Tertiary Mixture at a Fixed Purity Constraint.*** To examine a more complex separation, a ternary mixture consisting of α chymotrypsinogen A, ribonuclease A, and a later eluting artificial component is investigated in this section. We first develop the ANN-based hybrid model for all three components and then employ these models in SQP-based optimization. The optimization results for all three components are presented in Figure 6. Figure 6a presents the optimal values of production rate times yield of the tertiary mixture at a 95% purity constraint. The first component is the early eluting ribonuclease A, the second component is α chymotrypsinogen A, and the third component is the later eluting artificial component. It is important to note that the optimal values of the production rate times yield of the middle eluting component is below the optimal values of the other components, at all levels of loading since it experiences overlap from both the early and later eluting components. The maximal optimal value of the production rate times yield of the early eluting component occurs at a significantly higher loading than the later

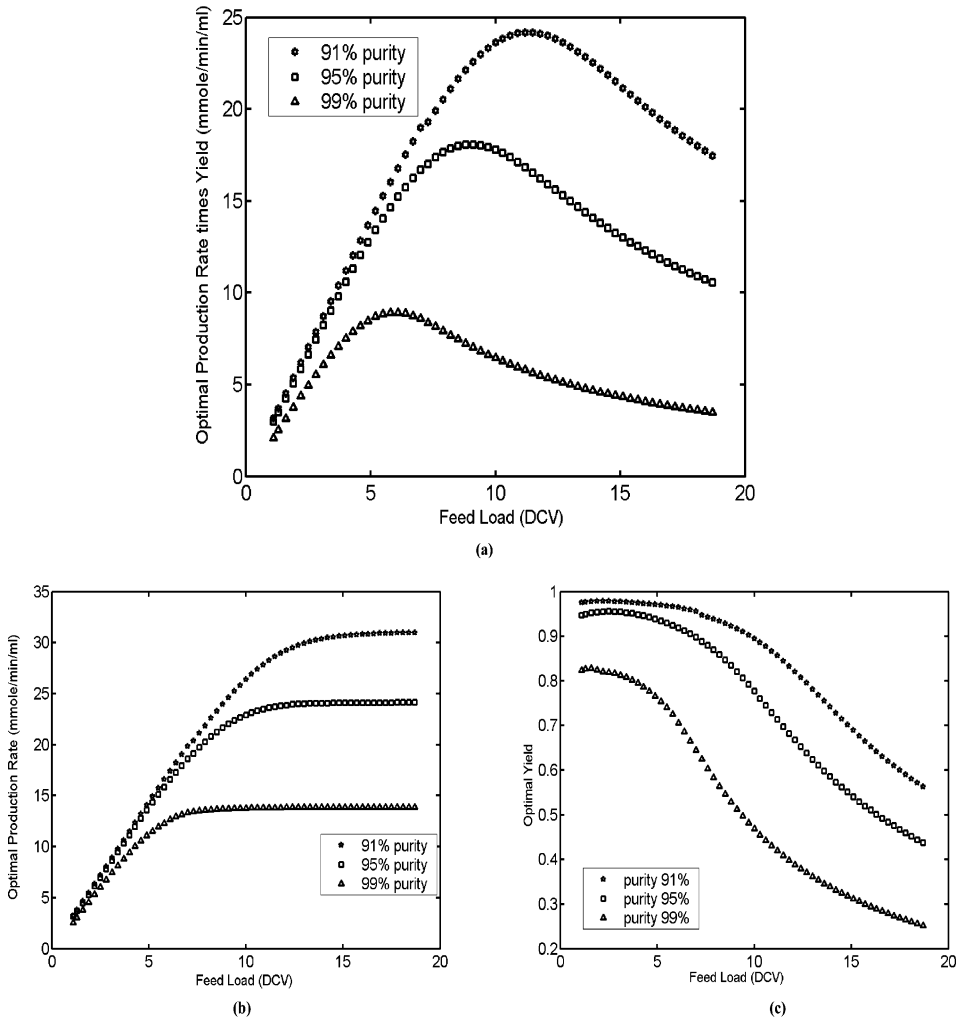

Figure 8. Optimization results for the later eluting component in a tertiary mixture at three different purities on a 90 μm FF Sepharose stationary phase: (☆) 91%, (□) 95%, and (△) 99% purity constraints. Column conditions: diameter 1.6 cm; length 10.5 cm. Feed conditions: ribonuclease A, α chymotrypsinogen A, and the artificial component at 0.5 mM each. All optimal results are presented as a function of column loadings (DCV). (a) Optimal production rate times yield (mmol/min/mL). (b) Optimal production rate (mmol/min/mL). (c) Optimal yield.

eluting component. The optimal production rates of the middle and later eluting components are lower than that of the early eluting component. Since the separation factor between the second and third components is relatively low, the column loading is restricted to moderate values for these components in order to attain higher production rates at moderate yields. Further, while sample displacement effects increase the yield of the early eluting component, the effect is less pronounced for the later eluting component. It is interesting to note that although there is a drop in the optimal production rate values at higher and medium loadings for the early and middle eluting component, the optimal production rate of the later eluting component is nearly constant at higher loadings. On the other hand, the most significant decrease of the yield with increased loading is observed for the later eluting component. The optimal flow rate decreases with increased loading (from medium to higher loadings) for the middle eluting component as a result of transport effects at higher loadings. For all of the components, the optimal gradient slope is at the lowest value from moderate to high loadings. The increase of the optimal gradient slope for the early eluting component at low loading conditions was observed to be less pronounced for tertiary systems as compared to binary systems.

Effect of Purity Constraints. In this section we investigate the effect of purity as an independent parameter on the optimal values of objective functions and decision variables of the later eluting artificial component. Optimal values are studied as a function of loading at purities of 91%, 95%, and 99%. We first develop the ANN-based hybrid model at these purity levels for the later eluting component and then use them in SQP-based optimization. Figure 7 shows that the generated hybrid models have excellent predictive ability for all purity levels. As seen in the figure, data is collected over a very wide range (e.g., yield data, from 5% to 100%). The optimum values of production rate times yield, production rate, and yield as a function of loading at purities of 91%, 95%, and 99% for the later eluting component are shown in Figure 8a−c, respectively. As seen in figures, the maximum value of the production rate times yield decreases with increasing purity. Correspondingly, there is a decrease in the optimal production rate and yield with increasing purity. Interestingly, the increase from 95% to 99% purity level has a noticeable difference when compared with a similar increase from 91% to 95% purity level; there is a sharp decrease in the maximum value of yield. At 99% purity the effect of feed load was much more pronounced, resulting in a significant shift toward lower yields (Figure 8c). In addition, at these purities the

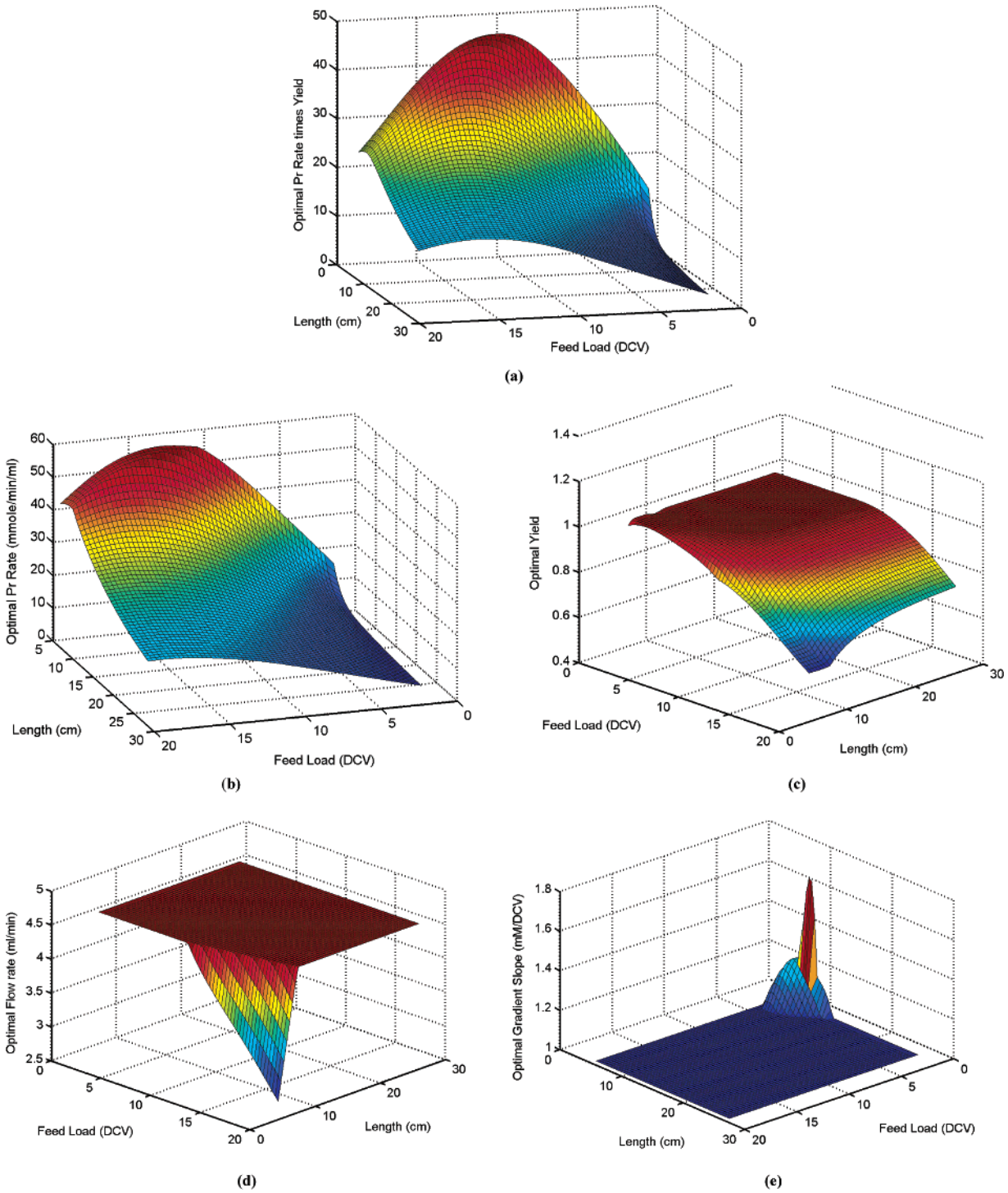

Figure 9. Optimization results as a function of column loadings and column design parameter (length) for an early eluting component for a tertiary mixture (α chymotrypsinogen A, ribonuclease A, and the later eluting artificial component on a 90 μm FF Sepharose stationary phase (at 95% puity levels). Column conditions: diameter 1.6 cm. Feed conditions: ribonuclease A, α chymotrypsinogen A, and the artificial component at 0.5 mM each. (a) Optimal production rate times yield (mmol/min/mL). (b) Optimal production rate (mmol/min/mL). (c) Optimal yield. (d) Optimal flow rate (mL/min). (e) Optimal gradient slope (mM/DCV).

optimum flow rates and optimum gradient slopes are relatively independent of the loading for the later eluting component (results not shown).

C. Simultaneous Design and Operating Condition Optimization. ***Tertiary Mixture at a Fixed Purity Constraint.*** To further illustrate the advantage of using a hybrid model framework, it was employed for simultaneous optimal column design and identification of optimal operating conditions for the ternary feed mixture. Hybrid models were developed between the outputs (production rate, yield, and maximum solute concentration) and inputs (flow rate, gradient slope, feed load, and column length) as described in the theory section. Figures 9, 10 and 11 present the optimization results at 95% purity for the early, middle, and later eluting components, respectively. In the figures, optimal results are presented as a function of column loadings and length.

Figure 9 presents the optimal results when production rate times yield of the early eluting component is optimized. As seen in Figure 9b, at higher loadings the optimal production rate first increases with an

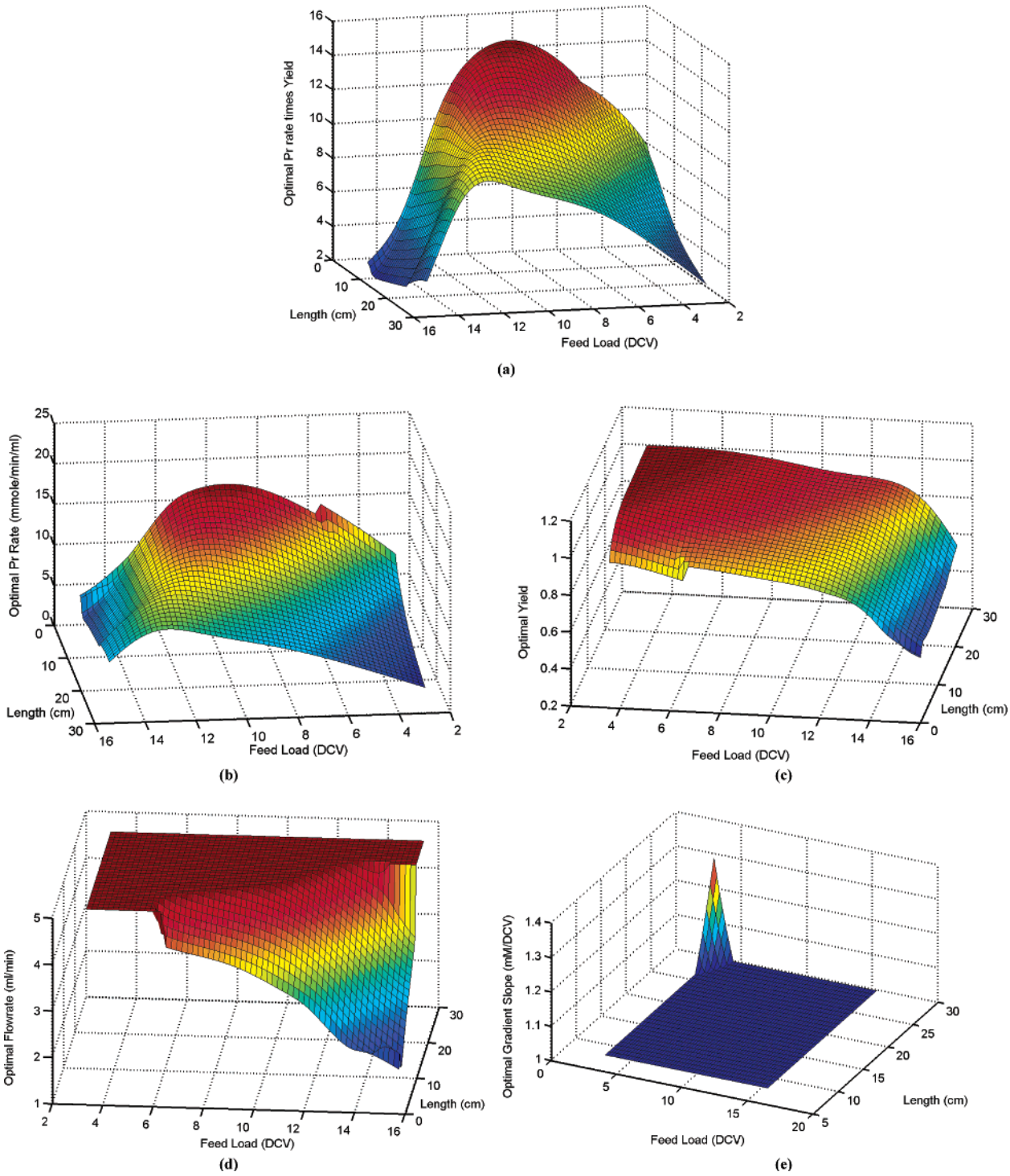

Figure 10. Optimization results as a function of column loadings and column design parameter (length) for the middle eluting component for a tertiary mixture (α chymotrypsinogen A, ribonuclease A, and the later eluting artificial component on a 90 μm FF Sepharose stationary phase (at 95% puity levels). Column conditions: diameter 1.6 cm. Feed conditions: ribonuclease A, α chymotrypsinogen A, and the artificial component at 0.5 mM each. (a) Optimal production rate times yield (mmol/min/mL). (b) Optimal production rate (mmol/min/mL). (c) Optimal yield. (d) Optimal flow rate (mL/min). (e) Optimal gradient slope (mM/DCV).

increase in length and then decreases when length is increased beyond its optimal value. The initial increase of the production rate with an increase in column length is due to the increased optimal flow rate with an increase in length. At lower lengths, flow rate has to be decreased to maintain higher yields. However, when the optimal flow rate reaches its maximum constrained value, any further increase in length causes a decrease of the production rate, because of the increased cycle time. For the same reason, at lower column loadings, production rate continuously decreases with an increase in length. Interestingly, at higher loadings yield increases with an increase in column length; however, it is essentially constant at lower loadings. As mentioned earlier, there is a drop in the optimal flow rate at higher loadings and lower column lengths. The optimal gradient slope is mostly constant at the lowest value, except for lower column lengths and loadings. In general, the optimal values of decision variables for this particular mixture at higher column lengths and loadings

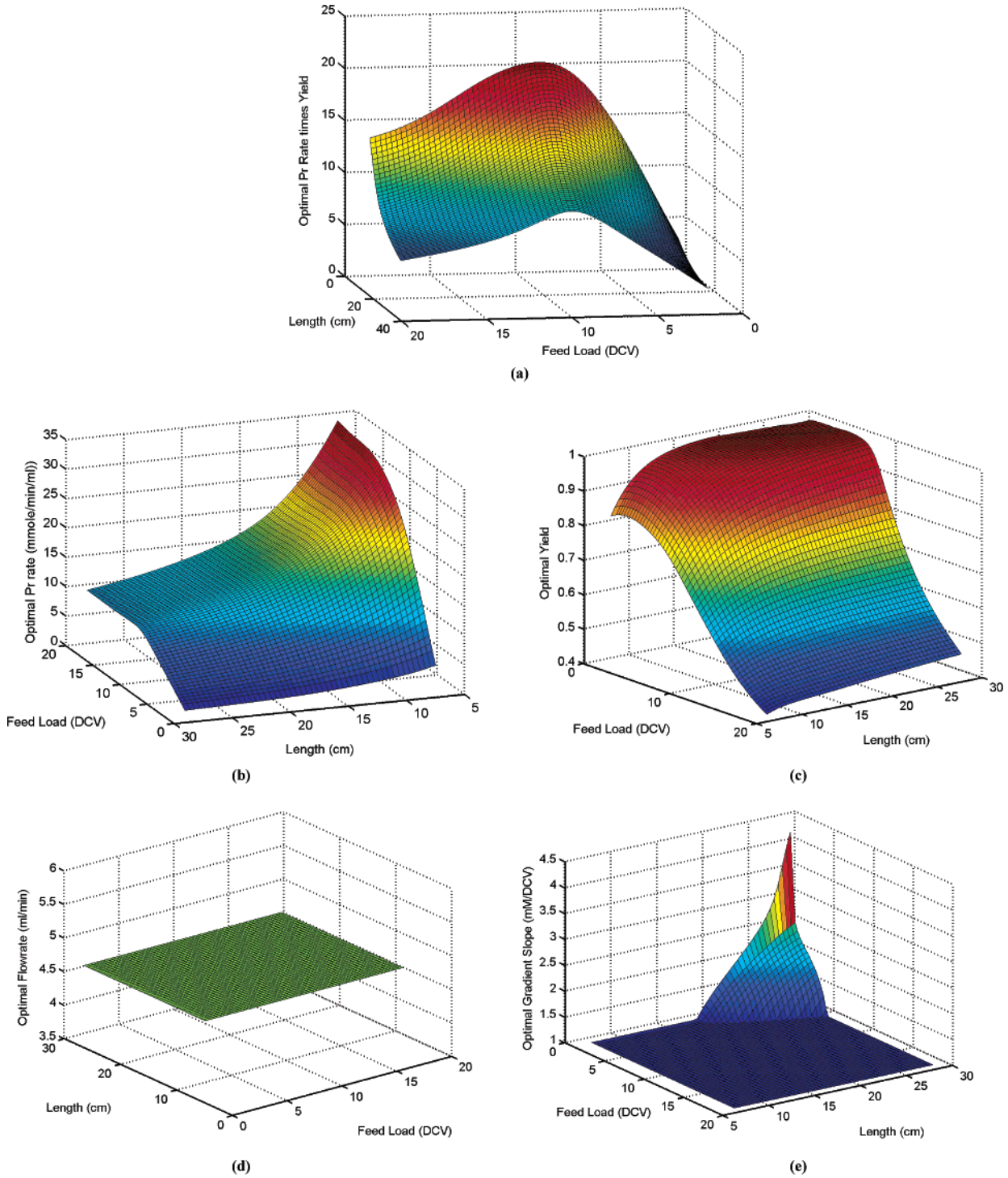

Figure 11. Optimization results as a function of column loadings and column design parameter (length) for the later eluting component in a tertiary mixture (α chymotrypsinogen A, ribonuclease A, and the later eluting artificial component on a 90 μm FF Sepharose stationary phase (at 95% puity levels). Column conditions: diameter 1.6 cm. Feed conditions: ribonuclease A, α chymotrypsinogen A, and the artificial component at 0.5 mM each. (a) Optimal production rate times yield (mmol/min/mL). (b) Optimal production rate (mmol/min/mL). (c) Optimal yield. (d) Optimal flow rate (mL/min). (e) Optimal gradient slope (mM/DCV).

were operation at higher flow rate and low gradient slope.

Figure 10 presents the optimal results when production rate times yield of the middle eluting component is optimized. As seen in Figure 10c, to attain a higher yield at medium to higher loadings for lower to higher column lengths, the flow rate was decreased from its maximal value significantly. Under these conditions, the optimal values of the flow rates are lower than when compared with the optimization results for the early eluting component. Again, this is because the overlap of the second component with the other two solutes and the low separation factor between individual components limits the flow rates to moderate values. Interestingly, there is a clear optimal value of production rate and production rate times yield at each column length, which is in sharp contrast to the scenario where the early eluting component is optimized. As seen in Figure 9b, optimal production rate experiences only a marginal decrease at higher loadings and higher lengths for the early eluting component. As was the case for the early eluting component, the optimal gradient slope is constant

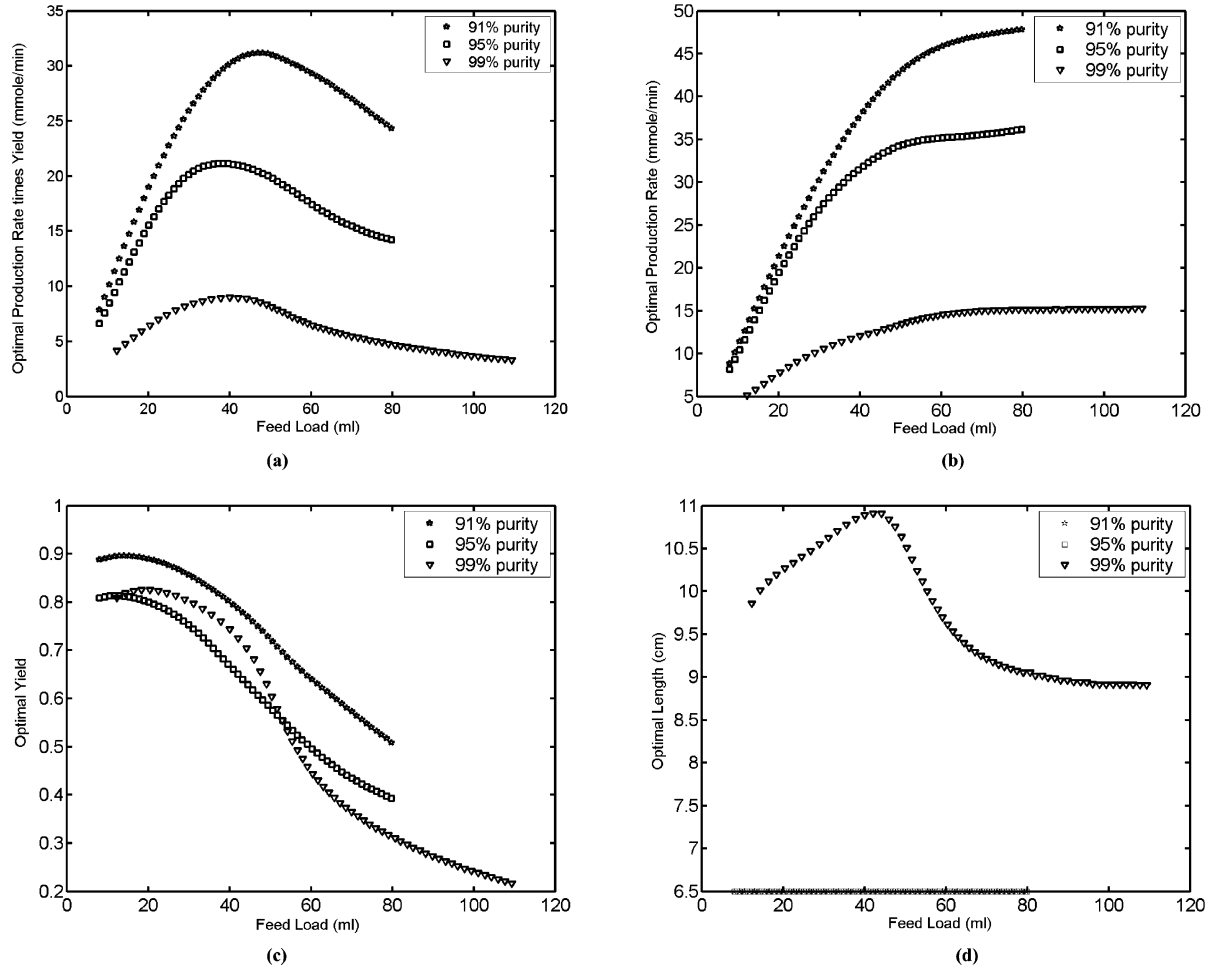

Figure 12. Optimization results for the later eluting component as a function of column loadings (mL) and column design parameter (length, cm), at three different purities for a tertiary mixture (α chymotrypsinogen A, ribonuclease A, and the later eluting artificial component) on a 90 μm FF Sepharose stationary phase. (☆) 91%, (□) 95%. and (▽) 99% purity constraints. Column conditions: diameter 1.6 cm. Feed conditions: ribonuclease A, α chymotrypsinogen A, and the artificial component at 0.5 mM each. (a) Optimal production rate times yield (mmol/min). (b) Optimal production rate (mmol/min). (c). Optimal yield.

at the lowest value, except for lower column lengths and loadings. The optimal values of decision variables for this particular mixture at higher column lengths and loadings were operation at medium flow rate and low gradient slope.

Figure 11 presents the optimal results when production rate times yield of the later eluting component is optimized. Interestingly, at higher column lengths the optimal production rate first increases with an increase in column loading and then remains essentially constant at higher loadings. As seen in the Figure 11b, to maintain higher production rates at higher column lengths and low loadings, the optimal gradient slope is maintained at higher values. The optimal values of decision variables for this particular mixture at higher column lengths and loadings were operation at high flow rate and low gradient slope.

The results shown in Figures 9−11 illustrate the significant differences in optimal behavior that can occur between early, middle, and later eluting components. It is also important to note that it would be computationally unreasonable to carry out this class of optimization using traditional physical models of preparative chromatographic systems.

Effect of Purity Constraints. The effect of purity as an independent design parameter on the simultaneous optimal column design and identification of optimal operating conditions was investigated for the later eluting component. Figure 12 presents the optimal results when length was also included as one of the decision variables in the optimization. This is in contrast to the results presented in the previous section (Figures 9−11) where length was not included in the decision variables for optimization and optimization results were presented at various column lengths and loadings. In the current case we can obtain an estimate of the optimal production rates, yields, flow rates, lengths, and gradient slopes at various levels of column loadings. Hybrid models were developed between the outputs (production rate, yield, and maximum solute concentration) and inputs (flow rate, gradient slope, feed load, and column length) at three levels (91%, 95%, and 99%) of purities. In Figure 12, optimal results are shown as a function of loadings in volume units (mL) in order to illustrate the effect of increased loading due to an increase in length. This is in contrast to the other results presented above where optimal results were shown as a function of dimensionless loading volume and column lengths.

As seen in Figure 12d, while higher column lengths are required to attain higher production rates and yields for 99% purity, the optimal column lengths at lower purity levels are at low values. In addition, the optimal

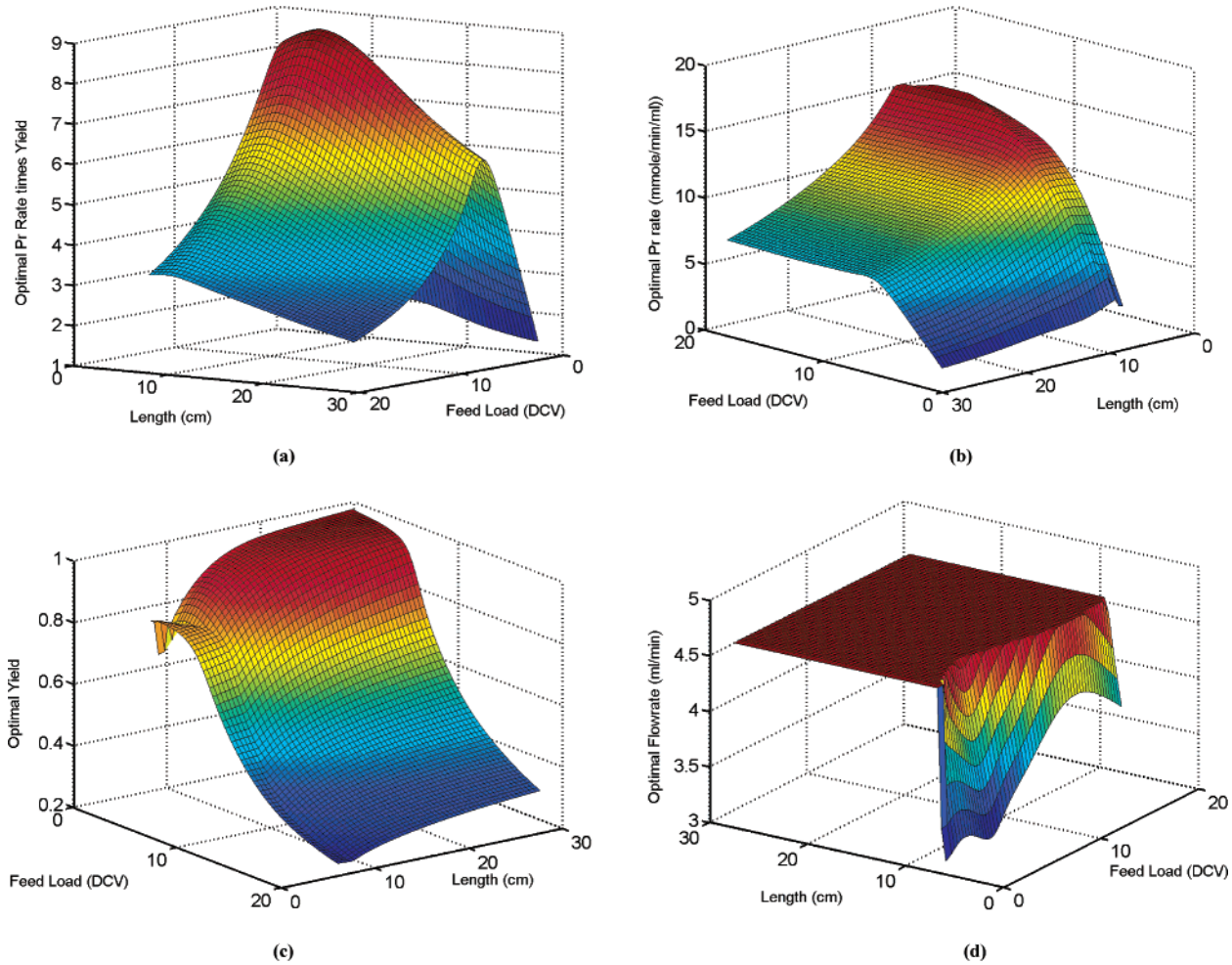

Figure 13. Optimization results as a function of column loadings and column design parameter (length) for the later eluting component for a tertiary mixture (α chymotrypsinogen A, ribonuclease A, and the later eluting artificial component on a 90 μm FF Sepharose stationary phase (at 99% puity levels). Column conditions: diameter 1.6 cm. Feed conditions: ribonuclease A, α chymotrypsinogen A, and the artificial component at 0.5 mM each. (a) Optimal production rate times yield (mmol/min/mL). (b) Optimal production rate (mmol/min/mL). (c) Optimal yield. (d) Optimal flow rate (mL/min).

column length first increases and then decreases with a continuous increase in loadings at 99% purity. Interestingly, at lower loadings, optimal yields at 99% purity are higher than those obtained at 95% purity. At all loadings, the production rate at 95% purity is higher than that obtained at 99% purity constraint.

To explain the initial increase and decrease of optimal column lengths with an increase in loadings at 99% purity level, we investigate the optimal surface as a function of column lengths and loadings at 99% purity constraint. Figure 13 presents the optimal surface results for the later eluting component at various column loadings and lengths at 99% purity. As seen in Figure 13b, at all loadings, the optimal production rate first increases and then decreases with a continuous increase in column lengths. Consequently, in Figure 12d optimal column length initially increases with an increase in loadings, to increase the optimal yields. However, it decreases later with a further increase in loadings to increase the optimal production rates. Interestingly, there is a clear difference in the variation of the optimal production rates with column lengths at 95% and 99% purity levels. At 95% purity level, optimal production rate continuously decreases at all column loadings with an increase in column lengths, whereas at 99% purity level there is a clear optima in column length. In addition, the optimum flow rates for the later eluting component (at 99% purity level) is a function of lower column lengths at all loadings.

5. Conclusions and Future Work

In this paper we have developed a hybrid model framework for optimization of preparative chromatographic processes. We have demonstrated that this strategy is well suited to address a large number of decision variables, permits the exploration of different design scenarios, and enables the straightforward coupling of optimal column design with optimal operating conditions. The hybrid model approach provides flexibility to the chromatographic engineer and dramatically reduces the computational time required for simulation and multivariable optimization. It also enables the estimation of optimal operating conditions, under different parametric specifications without any additional computational requirements. We have recently shown that this strategy is well suited for multiobjective optimization (Nagrath et al., 2002), which addresses the priorities and tradeoffs of various competing objectives and/or constraints in complex nonlinear chromatographic systems. Future work will employ this hybrid model approach in concert with the GR2R nonlinear control method recently developed by the authors (Nagrath et

Table 3. Dimensionless Variables Formed for the General Rate Model

$\tau = t / L/u_0$	$z = x / L$	$\xi = r / R$	$C_{bi} = c_{bi} / C_{fi}$	$C_{pi} = c_{pi} / C_{fi}$
$\Phi_{ki} = (1 - \epsilon_p)q_{\max\, i} / \epsilon_p C_{fi}$		$Pe_i = u_0 L / D_{ai}$		$B_{fi} = k_{fi} L / \epsilon_p R u_0$
$N_{fi} = 3L / R\,(1 - \epsilon_b)k_{fi} / \epsilon_b u_0$		$N_{pi} = D_{pi} L / u_0 R^2$		$N_{si} = D_{si} L / u_0 R^2$
$Y_{li} = y_{li} L / q_{\max i} u_0$				

al., 2003) for improving the performance of large-scale chromatographic processes by reducing batch-to-batch variations.

Notation

c_i	mobile phase concentration (mM)
c_{fi}	feed concentration (mM)
c_{p1}	pore phase salt concentration (mM)
D_{ai}	axial dispersion coefficient (cm^2/s)
D_{pi}	pore diffusion coefficient (cm^2/s)
D_{si}	surface diffusion coefficient (cm^2/s)
k_{fi}	film mass transfer coefficient (cm/s)
k_{di}	adsorption rate constant ($mM^{-\nu}/s$)
k_{di}	desorption rate constant ($mM^{-\nu}/s$)
K_{SMA}	steric mass action isotherm equilibrium constant
L	length of column (cm)
q_i	stationary phase concentration (mM)
$\bar{q}_1$	concentration of bound salt that is not sterically shielded (mM)
q_1	total bound concentration of salt on the stationary phase (mM)
R	particle radius (cm)
u_o	interstitial velocity (cm/s)
x	axial distance (cm)
r	radial distance inside the particle (cm)

Greek letters

ϵ_i	interstitial porosity
ϵ_p	particle porosity
ν_i	characteristic charge for ith component
σ_i	steric factor
Λ	ionic capacity (mM)

Appendix

A. Dimensionless Equations. Equations 1−11 can be converted into a nondimensional form using the following dimensionless variables presented in Table 3.

The dimensionless equations for the generalized model are

$$\frac{\partial C_{bi}}{\partial \tau} = \frac{1}{P_{ei}}\frac{\partial^2 C_{bi}}{\partial z^2} - \frac{\partial C_{bi}}{\partial z} - N_{fi}[C_{bi} - C_{pi}(\xi = 1)] \quad (18)$$

$$\frac{\partial C_{pi}}{\partial \tau} = N_{pi}\nabla_s^2 C_{pi} - \Phi_{ki} Y_{li} \quad (19)$$

The Laplacian $\nabla_s^2 C$ used in eq 19 is defined as

$$\nabla_s^2 C = \frac{1}{z^2}\frac{\partial}{\partial}\left(z^2 \frac{\partial C}{\partial z}\right)$$

where subscript s indicates that the domain is spherical.

$$K_i \frac{\partial \theta_i}{\partial \tau} = K_i N_{si} \nabla \theta_i + \Phi_{ki} Y_{li} \quad (20)$$

where subscript n denotes the component.

Boundary conditions:

$$\frac{\partial C_{bi}}{\partial z} = \begin{bmatrix} Pe_i[C_{bi} - C_{fi}] & z = 0 \\ 0 & z = 1 \end{bmatrix} \quad (21)$$

$$N_{pi}\frac{\partial C_{pi}}{\partial \xi} + K_i N_{si}\frac{\partial \theta_i}{\partial \xi} = \langle Pe_i[C_{pi} - C_{fi}]\ \xi = 1\rangle$$

$$2K_i N_{si}\frac{\partial \theta_i}{\partial \xi} = K_i \frac{\partial \theta_i}{\partial \tau} - \Phi_{ki} Y_{li} \xi = 1 \quad (22)$$

B. Bulk Phase Discretized Equations. To derive the weak form of the above eq 18, the differential form is first multiplied by a smooth weighting function W belonging to a space of functions, $W \epsilon W_h^k$. The resulting product is then integrated over an open space-time domain Ω. Integration by parts then transfers the spatial derivatives from the fluxes on to the weighting function, thus decreasing the continuity requirements of the solution. In turn boundary integrals appear in the weak form. The weighted residual form of the bulk phase equation can be written as

$$\int_{\Omega^e} W^h \left(\frac{\partial C_{bn}}{\partial \tau} - \frac{1}{P_{en}}\frac{\partial^2 C_{bn}}{\partial z^2} + \frac{\partial C_{bn}}{\partial z} + N_{fn}[C_{bn} - C_{pn}(\xi = 1)] \right) d\Omega^e = 0 \quad (23)$$

where $\Omega.^e$ is the finite element domain. The integration by parts of the second order differential terms leads to the following weak form:

$$\int_{\Omega^e} W^h C^h_{bn,t} + \frac{1}{P_{en}}\int_{\Omega^e} W^h_{,i}\, C^h_{bn,i} d\Omega^e - \frac{1}{P_{en}} W^h C^h_{bn,i}|_{\Gamma^e} + \int_{\Omega^e} (W^h C^h_{bn,i} + N_{fn} W^h C^h_{bn}) d\Omega^e - \int_{\Omega^e} N_{fn} W^h C_{pn}(\xi = 1) d\Omega^e = 0 \quad (24)$$

where C^h_{bn}, W^h are interpolated using shape functions over an element as $C^h_{bn} = \sum_{A=1}^{nnp} N_A C^A_{bn}$, $C^h_{bn,i} = \sum_{A=1}^{nnp} N_{A,i} C^A_{bn}$, and $W^h = \sum_{A=1}^{nnp} N_A D_A$. Since the interpolating functions are chosen to be same for both the solution and weight space, it leads to a Galerkin form. After substituting C^h_{bn}, W^h with the interpolating functions, a set of nonlinear ordinary differential equations are obtained which in the matrix form can be expressed as

$$[M_n][C'_{bn}] = [K_n][C_{bn}] + [B_n] + [F_n] C_{pn}(\xi = 1) \quad (25)$$

C. Particle Phase Discretized Equations. Using orthogonal collocation on finite elements the above equa-

tions are discretized for element l and collocation point i as

$$\frac{dC_{pn,i}}{d\tau} = N_{pi}\frac{1}{h_l}\left\{\sum_{j=1}^{NCOL+2} B_{i,j}C_{pn,j} + \frac{2}{r_l}\sum_{j=1}^{NCOL+2} A_{i,j}C_{pn,j}\right\} + \Phi_{kn}Y_{ln,i} \quad (26)$$

$$K_{n,i}\frac{d\theta_{n,i}}{d\tau} = K_n N_{sn,i}\left\{\sum_{j=1}^{NCOL+2} B_{i,j}\theta_{n,j} + \frac{2}{r_l}\sum_{j=1}^{NCOL+2} A_{i,j}\theta_{n,j}\right\} + \Phi_{kn}Y_{ln,i} \quad (27)$$

For the l th element,

$$r_l = \frac{\xi - \xi_l}{h_l}\, h_l = \xi_{l+1} - \xi_l$$

The discretized boundary conditions for the pore and the solid phase can be represented as

Boundary conditions:

$$N_{pi}\frac{\partial C_{pi}}{\partial \xi} + K_i N_{si}\frac{\partial \theta_i}{\partial \xi} = \langle Pe_i[C_{pi} - C_{fi}];\ \xi = 1\rangle$$

$$2K_i N_{si}\frac{\partial \theta_i}{\partial \xi} = K_i\frac{\partial \theta_i}{\partial \tau} - \Phi_{ki}\, Y_{li};\ \xi = 1$$

$$\sum_{NCOL+2}^{j=1} A_{ij}C_{pn,j} = 0\ \langle \epsilon = 0|$$

$$\sum_{NCOL+2}^{j=1} A_{ij}C_{pn,j} = 0\ \langle \epsilon = 0| \quad (28)$$

References and Notes

(1) Brooks, C. A.; Cramer, S. M. Steric mass-action ion-exchange: Displacement profiles and induced salt gradients. *AIChE J*. **1992**, *38*(12), 1969−1978.

(2) Ernest, M. V.; Whitley, R. D., Jr.; Ma, Z.; Wang, N.-H. L. Effects of mass action equilibria on fixed-bed multicomponent ion exchange dynamics. *Ind. Eng. Chem. Res.* **1997**, *36*(1), 212−226.

(3) Felinger, A.; Guiochon, G. Comparison of maximum production rates and optimum operating/design parameters in overloaded elution and displacement chromatography. *Biotechnol. Bioeng.* **1993**, *41*, 134−147.

(4) Felinger, A.; Guiochon, G. Optimizing experimental conditions in overloaded gradient elution chromatography. *Biotechnol. Prog.* **1996**, *12*(5), 638−644.

(5) Gallant, S. R.; Kundu, A.; Cramer, S. M. Optimization of step gradient separations: Consideration of nonlinear adsorption. *Biotechnol. Bioeng.* **1995**, *47*(3), 355−372.

(6) Gallant, S. R.; Vunnum, S.; Cramer, S. M. Optimization of preparative ion-exchange chromatography of proteins: Linear gradient separations. *J. Chromatogr. A* **1996**, *725*(2), 295−314.

(7) Guiochon, G.; Golshan-Shirazi, S.; Katti, A. M. *Fundamentals of Preparative and Nonlinear Chromatography*; Academic Press: New York 1994.

(8) Gu, T.; Tsao, G. T.; Ladisch, M. R. Displacement effect in multicomponent chromatography. *AIChE J.* **1990**, *36*(8), 1156−1162.

(9) Luo, R. G.; Hsu, J. T. Optimization of gradient profiles in ion-exchange chromatography for protein purification. *Ind. Eng. Chem. Res.* **1997**, *36*, 444−450.

(10) Ma, Z.; Whitley, R. D.; Wang, N.-H. L. Pore and surface diffusion in multicomponent adsorption and liquid chromatography systems. *AIChE J.* **1996**, *42*(5), 1244−1262.

(11) MacKay, D. J. C. Bayesian interpolation. *Neural Comput.* **1992**, *4*, 415−447.

(12) Nagrath, D.; Messac, A.; Bequette, B. W.; Cramer, S. M. Physical programming based multiobjective optimization strategies for chromatographic processes. *AIChE J.* **2002**, submitted for publication.

(13) Nagrath, D.; Bequette, B. W.; Cramer, S. M. Evolutionary operation and control of chromatographic processes. *AIChE J.* **2003**, *49*(1), 82−95.

(14) Natarajan, V.; Cramer, S. M. Modeling shock layers in ion-exchange displacement chromatography. *AIChE J.* **1999b**, *45*(1), 27−37.

(15) Natarajan, V.; Bequette, B. W.; Cramer, S. M. Optimization of ion-exchange displacement separations I. Validation of an iterative scheme and its use as a methods development tool. *J. Chromatogr. A* **2000**, *876*(1−2), 51−62.

(16) Natarajan, V.; Cramer, S. M. A Methodology for the characterization of ion-exchange resins. *Sep. Sci. Technol.* **2000a**, *35*(11) 1719−1742.

(17) Natarajan, V.; Cramer, S. M. Optimization of ion-exchange displacement separations II. Comparison of displacement separations on various ion-exchange resins. *J. Chromatogr. A* **2000b**, *876*(1−2), 63−73.

(18) Natarajan, V.; Ghose, S.; Cramer, S. M. Comparison of linear gradient and displacement separations in ion-exchange systems. *Biotechnol. Bioeng.* **2002**, *78*(4) 365−375.

(19) Petzold, L. R. *DASSL: A Differential/Algebraic System Solver*; Lawrence Livermore National Laboratory: Livermore, CA, 1982.

(20) Saunders, M. S.; Vierow, J. B.; Carta, G. Uptake of phenylalanine and tyrosine by a strong-acid cation exchanger. *AIChE J.* **1989**, *35*(1), 53−68.

(21) Suwondo, E.; Wilhelm, A. M.; Pibouleau, L.; Domenech, S. Optimization of a liquid chromatographic separation process. *Comput. Chem. Eng.* **1993**, *17*, S135−S140.

(22) Yoshida, H.; Yoshikawa, M.; Kataoka, T. Parallel transport of BSA by surface and pore diffusion in strongly basic chitosan. *AIChE J.* **1994**, *40*(12), 2034−2044.

Accepted for publication September 5, 2003.

BP034026G